ACSNANO

www.acsnano.org

Article

Sliding Ferroelectricity in MoS_2/ReS_2 Heterojunction for a Sensitive and Reconfigurable Bioelectronic Interface

Weijia Mu, Changming Ke,* Ning Guo, Zheng Zhang, Lei Yang, Zhewei Li, Yaming Zhou,* Jing Li, Shufang Yue, Jingying Zheng, Qiang Zheng, Shi Liu, and Liying Jiao*

Cite This: https://doi.org/10.1021/acsnano.6c01271

Read Online

ACCESS | Metrics & More | Article Recommendations | Supporting Information

ABSTRACT: Two-dimensional (2D) sliding ferroelectrics promise an ultrathin, fatigue-free platform for reconfigurable electronics, but their development has been hindered by a strict requirement for lattice matching, which limits the material choice and functionality. Here, we overcome this limitation by demonstrating room-temperature sliding ferroelectricity in a lattice-mismatched semiconducting MoS_2/ReS_2 heterobilayer. This van der Waals semiconductor displays robust switchable resistive states with submicrosecond dynamics and an endurance exceeding 10^5 cycles. Building on these properties, we developed a ferroelectric field-effect transistor-based biosensor (bio-FeFET) for label-free detection of 8-hydroxy-2′-deoxyguanosine (8-OHdG), a key biomarker for oxidative DNA damage. The polarization-induced field enhances electrostatic enrichment of negatively charged aptamers, achieving high sensitivity and an ultralow limit of detection (LoD). Importantly, polarization reversal enables a reconfigurable "write−read−erase" operation, thereby allowing the electrical regeneration of the sensing interface without chemical treatment. These findings not only broaden the material horizon for sliding ferroelectrics but also support the development of high-sensitivity, reconfigurable bioelectronic interfaces for logic-integrated sensing.

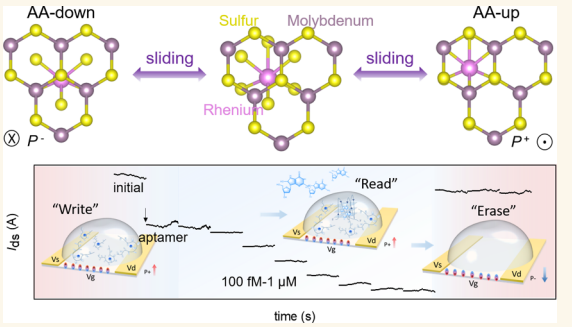

KEYWORDS: *two-dimensional, semiconductor, heterojunction, ferroelectricity, biosensing*

INTRODUCTION

The recent discovery of sliding ferroelectricity in stacked transition metal dichalcogenides (TMDCs) has established a new class of ferroelectric semiconductors.[1−3] These materials uniquely integrate spontaneous polarization with gate-tunable transport, thereby redefining the application landscape for two-dimensional (2D) semiconductors beyond conventional field-effect transistors (FETs) to include reconfigurable electronics, nonvolatile memory, and ferroelectric photovoltaics.[4−6] However, the practical realization of this phenomenon is currently constrained by stringent material requirements. To date, sliding ferroelectricity has been predominantly observed in homobilayers or few-layer systems composed of identical materials, such as 3R-MoS_2[7,8] and InSe,[9−11] with the exception of the MoS_2/WS_2 heterobilayer that exhibits near-perfect lattice matching (mismatch <0.3%).[12] This critical dependence on lattice alignment severely limits the selection of available material combinations, thereby restricting both the material diversity and the tunability of interfacial properties. Furthermore, the applications of sliding ferroelectricity have been largely limited to device prototypes such as ferroelectric tunneling junctions (FTJs)[9,13,14] and ferroelectric FETs (FeFETs)[8,15,16] for nonvolatile, reconfigurable logic. Beyond these applications, the reversible polarization of sliding ferroelectrics provides a means to modulate surface charge states, presenting unexplored opportunities for high-sensitivity, reconfigurable, and reliable bioelectronic interfaces. In such interfaces, the adsorption and desorption of charged biomolecules can be actively programmed by polarization,[17] enabling dynamic control over sensing processes.

To expand the material systems and biosensing applications of 2D sliding ferroelectric semiconductors, we designed a lattice-mismatched MoS_2/ReS_2 semiconducting heterobilayer guided by density functional theory (DFT) calculations. The atomic structures and the ferroelectricity of the bilayer were comprehensively characterized by scanning transmission electron microscopy (STEM), second-harmonic generation (SHG), and piezoresponse force microscopy (PFM). Electrical measurements revealed reliable bistable resistive switching with an ultrafast response (<1 μs) and high endurance (>10^5 cycles), demonstrating robust, fatigue-free operation. Leveraging these properties, we fabricated a bio-FET with the bilayer for the label-free detection of 8-hydroxy-2′-deoxyguanosine (8-

Received: January 21, 2026
Revised: April 17, 2026
Accepted: April 20, 2026

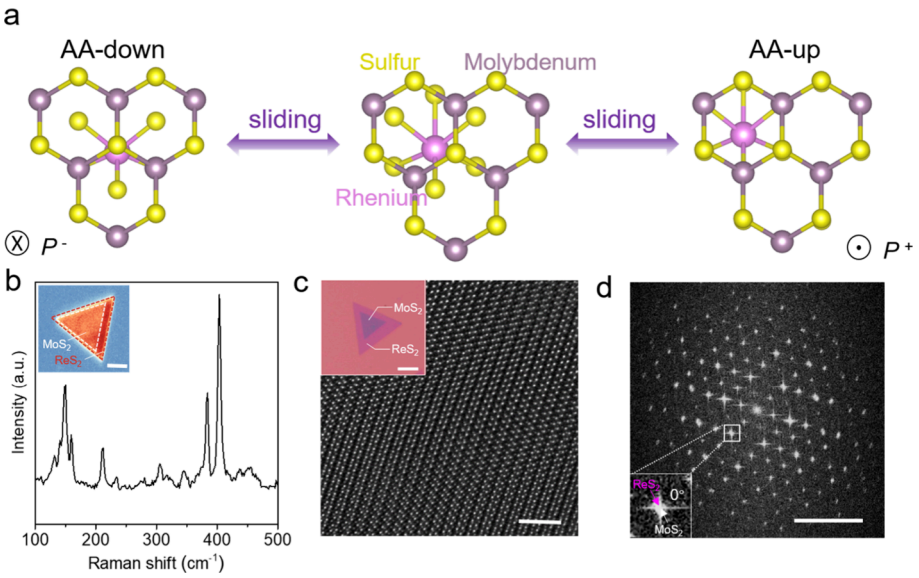

Figure 1. DFT calculations on the polarization and structural characterizations of the MoS_2/ReS_2 heterojunction. (a) Schematic illustration of polarization reversal in the MoS_2/ReS_2 heterojunction. AA-down and AA-up stackings create out-of-plane ferroelectric polarization in opposite directions, which can be switched by the interlayer sliding motion. The central panel shows the intermediate sliding process. Molybdenum, rhenium, and sulfur atoms are displayed in purple, magenta, and yellow, respectively. (b) Typical Raman spectrum collected on the bilayer MoS_2/ReS_2. Inset: corresponding Raman mapping of a MoS_2/ReS_2 heterojunction, scale bar: 10 μm. (c) Representative HAADF-STEM image of the MoS_2/ReS_2 bilayer, scale bar: 2 nm. Inset: corresponding optical image of the bilayer, scale bar: 10 μm. (d) Diffraction patterns of the MoS_2/ReS_2 heterojunction obtained through fast Fourier transform (FFT) analysis of the STEM image, scale bar: 5 1/nm. The white box marks the region where diffraction spots from the two lattices are perfectly aligned, indicating a 0° rotational alignment between the monolayers. The enlarged inset in the lower left corner provides a closer view of the overlapping diffraction spots, with magenta and white arrows indicating lattice spots corresponding to ReS_2 and MoS_2, respectively.

OHdG), a biomarker for oxidative DNA damage.[18,19] The operation of the device is governed by the built-in polarization field within the bilayer, which enhances the adsorption of charged biomolecules. This mechanism not only significantly improves the detection sensitivity but also enables a reconfigurable "write−read−erase" functionality for the regeneration of the sensing interface. Our findings thus expand the material space for sliding ferroelectrics and establish a paradigm for high-sensitivity, reconfigurable bioelectronic interfaces applicable to logic-integrated and adaptive biomedical applications.

RESULTS AND DISCUSSION

Design and Construction of a Lattice-Mismatched Sliding Ferroelectric

We explore the extension of sliding ferroelectricity to nonlattice-matched 2D semiconductors by investigating the MoS_2/ReS_2 heterobilayer as a model system. First-principles calculations were performed on its parallel-aligned (0° twist) configuration, which features two energetically comparable stacking registries: AA-down and AA-up (Figure 1a). These two states are connected by the canonical sliding path, a one-third unit-cell translation along the armchair direction (Figure S1), which breaks the interfacial mirror symmetry. This symmetry breaking induces a switchable out-of-plane polarization, as supported by a finite interfacial dipole moment in differential charge density (DCD) analysis (Figure S3). DFT calculations reveal that the transition between AA-down and AA-up states involves a low energy barrier of ~6.2 meV per formula unit, comparable to that of established sliding ferroelectrics such as bilayer hBN (Figure S2).[20] The spontaneous polarization emerges from the charge redistribution induced by this registry change, with the polarization direction switching between upward and downward as the system slides between the two configurations. Importantly, the inherent lattice mismatch between MoS_2 and ReS_2 (1.40% along the *a*-axis and 2.32% along the *b*-axis) in this heterostructure introduces interfacial strain that modulates the sliding potential, potentially enhancing the stability of the bistable states (Figures S4 and S5). The low switching barrier, combined with minimal ionic displacement and reduced charge trapping at the interface, suggests strong potential for fatigue-resistant ferroelectric performance.

To experimentally verify our theoretical predictions, we fabricated a van der Waals heterostructure by dry-transferring a high-quality chemical vapor deposition (CVD)-grown monolayer of ReS_2 onto a CVD-grown monolayer of MoS_2 (Figures S6 and S7). The resulting heterostructure was subsequently characterized by using a combination of microscopic and spectroscopic techniques to assess its structural quality and stacking alignment. High-angle annular dark-field (HAADF)-STEM imaging revealed the atomic structure of the heterojunction, displaying periodic moiré fringes that arise from the lattice mismatch between MoS_2 and ReS_2 (Figure 1c and Figure S9). The obtained images directly indicate high-quality stacking with a well-defined interlayer registry. The corresponding electron diffraction pattern (Figure 1d) further confirmed the 0° stacking configuration and high crystallinity, showing two sets of sharp, well-aligned diffraction spots corresponding to the individual layers. To probe the interlayer coupling, we conducted Raman and photoluminescence (PL) spectroscopic measurements on both the monolayer and heterojunction regions. In the heterobilayer region, the Raman spectrum of MoS_2 showed an increased peak separation of 20 cm^{-1} between the E^1_{2g} and A_{1g} modes, compared to 18 cm^{-1} in

https://doi.org/10.1021/acsnano.6c01271
ACS Nano XXXX, XXX, XXX−XXX

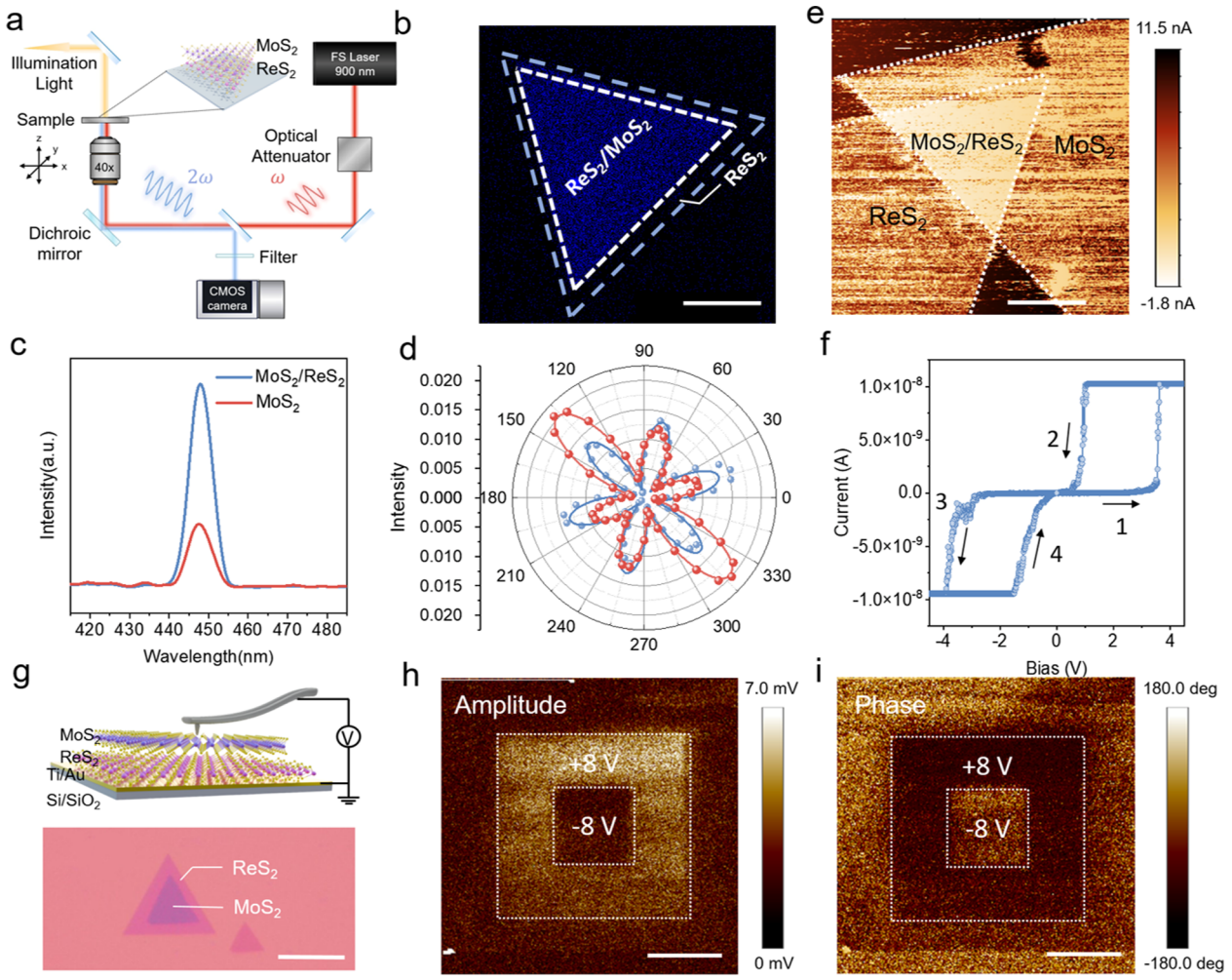

Figure 2. Ferroelectricity characterization of the MoS_2/ReS_2 heterojunction. (a) Schematic diagram of the SHG characterization setup. (b) SHG intensity mapping image of MoS_2/ReS_2 heterojunction, scale bar: 20 μm. (c) SHG spectra of monolayer MoS_2 (red line) and the MoS_2/ReS_2 heterojunction (blue line). (d) Polarization-resolved SHG intensity for monolayer MoS_2 (blue dashed line) and the MoS_2/ReS_2 heterojunction (red dashed line). (e) C-AFM current mapping of the Pt/MoS_2−ReS_2/Pt device. The dashed lines outline the MoS_2 and ReS_2 regions, scale bar: 5 μm. (f) I−V curves from C-AFM measurements of the Pt/MoS_2−ReS_2/Pt device. (g) Upper: schematic diagram of the PFM measurement setup; lower: optical image of the sample used for PFM measurements; scale bar: 20 μm. (h) PFM amplitude and (i) out-of-plane (OOP) phase images of the MoS_2/ReS_2 heterojunction after electrical poling. The white box-in-box patterns were written by applying −8 V and +8 V poling voltages, scale bars: 2 μm.

the monolayer MoS_2,[21] suggesting enhanced interlayer coupling and charge redistribution.[22] Additional peaks characteristic of ReS_2 were also observed (Figure 1b).[23,24] PL measurements revealed a significant blueshift and quenching of the emission peak in the heterobilayer region (Figure S8), compared to its prominent peak at 682 nm (1.82 eV) in the monolayer region.[25] This suppression of radiative recombination suggests efficient electron−hole separation at the interface driven by interlayer charge transfer.[26,27]

Room-Temperature Ferroelectricity of MoS_2/ReS_2 Heterojunction

To investigate the structural basis for potential sliding ferroelectricity, we carried out SHG measurements on the stacked heterobilayer (Figure 2a). As expected, monolayer MoS_2 (D_{3h} symmetry, noncentrosymmetric) exhibited a strong SHG response,[28] whereas centrosymmetric monolayer ReS_2 (C_i symmetry) showed a negligible SHG signal (Figure S10).[29] The MoS_2/ReS_2 heterojunction displayed a pronounced SHG with sharp boundaries (Figure 2b,c). The SHG intensity exhibited a quadratic dependence on excitation power, confirming its second-order nonlinear origin (Figure S12). Polarization-resolved SHG measurements further revealed identical 6-fold petal patterns for both monolayer MoS_2 and the MoS_2/ReS_2 heterojunction, suggesting a well-aligned, twist-free stacking (Figure 2d).[30,31] Notably, the SHG intensity in the heterojunction region exhibited a pronounced SHG signal with distinct angular anisotropy, indicating symmetry breaking and interlayer coupling at the interface (Figure S11).[32] Collectively, these SHG results demonstrate the breakdown of spatial inversion symmetry at the interface of the bilayer, a critical structural prerequisite for sliding ferroelectricity. We then directly probed the ferroelectric properties of the heterojunction by using PFM (Figure 2g and Figure S15). As shown in Figure 2h,i, clear polarization switching was observed in the heterojunction through reversible phase and amplitude contrast under tip bias voltages of ±8 V, with no associated morphological changes (Figure S16). This ferroelectric response is intrinsic to the interface, as no switching was detected in the individual monolayer MoS_2

https://doi.org/10.1021/acsnano.6c01271
ACS Nano XXXX, XXX, XXX−XXX

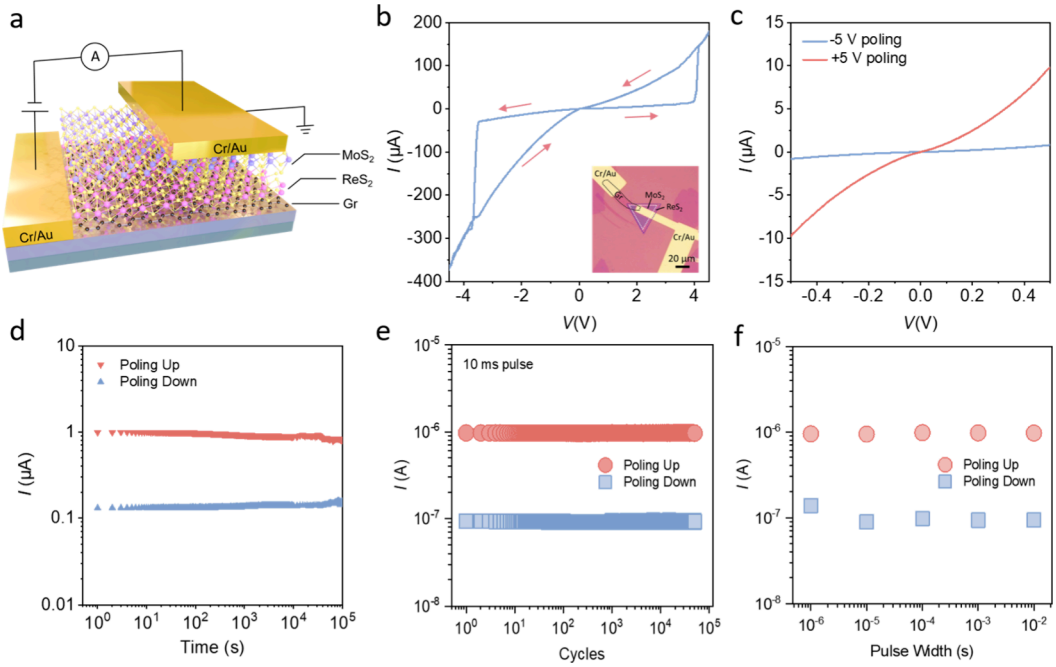

Figure 3. Tunneling current characterization of the FTJ device. (a) Schematic illustration of an FTJ based on the MoS_2/ReS_2 heterojunction. (b) $I-V$ characteristics of the FTJ device demonstrate tunneling electroresistance between the LRS and HRS states, which are set by applying +4.0 V and −3.5 V poling voltages, respectively. The arrows indicate the direction of the current change. Inset: the corresponding optical image, where the black dotted line delineates the bottom graphene electrode and purple and white dotted lines delineate ReS_2 and MoS_2, respectively. (c) Polarization-dependent tunneling current versus the applied DC field through the FTJ device. (d) Retention properties of the bistate after applying +5 V and −5 V poling voltages. (e) Fatigue analysis of the FTJ over 10^5 switching cycles with a 10 ms pulse width. (f) Current of HRS and LRS under varying pulse widths (1 μs, 10 μs, 100 μs, 1 ms, and 10 ms) with the same read voltage applied.

or ReS_2 (Figure S17). Furthermore, the stability of the written domains ruled out nonferroelectric artifacts such as electrostatic charging (Figure S16),[33,34] confirming the intrinsic ferroelectric nature of the MoS_2/ReS_2 heterojunction.

Polarization-Mediated Electrical Transport in the Sliding Ferroelectric Heterojunction

Having established the intrinsic ferroelectricity of the MoS_2/ReS_2 heterojunction, we then investigated the polarization-induced electrical transport characteristics in the heterojunction. To this end, we employed two complementary techniques: conductive atomic force microscopy (C-AFM) for nanoscale probing and FTJ devices for device-level assessment. Both methods rely on the same physical mechanism: tunneling conduction modulated by polarization-induced variations in the interfacial potential profile. At the nanoscale, C-AFM measurements on a Pt/MoS_2−ReS_2/Pt stack directly confirmed the ferroelectric switching behavior (Figure S13). C-AFM mapping under a small readout bias showed uniformly suppressed current in the MoS_2/ReS_2 region compared with individual monolayers, evidencing interfacial modulation of conductance (Figure 2e). As shown in Figure 2f and Figure S14, current−voltage ($I-V$) sweeps revealed a pronounced counterclockwise hysteresis, with reversible transitions between a high-resistance state (HRS) and a low-resistance state (LRS) at coercive voltages of approximately +4.0 V and −3.0 V. This observation validates the nonvolatile, out-of-plane polarization switching at the local interface. To assess device-level functionality, we fabricated FTJ devices by integrating a MoS_2/ReS_2 heterojunction between a graphene bottom electrode and a Cr/Au top electrode (Figure 3a and Figure S18). Electrical measurements revealed a pronounced counterclockwise hysteresis in the $I-V$ characteristics under DC bias sweeping (Figure 3b). Upon reaching a DC bias of 4.0 V, which corresponds to the coercive field of the MoS_2/ReS_2 heterojunction, the current underwent an abrupt transition from 18.1 to 134.9 μA, indicating a shift from the HRS to the LRS. Conversely, reversing the bias beyond −3.5 V induced the opposite transition, from LRS back to HRS. To confirm its nonvolatile behavior, the FTJ was poled with ±5 V for 10 s and subsequently read at a low-bias sweep (−0.5 to 0.5 V) or at a fixed 0.1 V, revealing two distinct resistance states that were stable for over 10^5 s (Figure 3c,d). We next investigated the dynamic switching and fatigue characteristics by applying voltage pulses with varying widths (1 μs to 10 ms). Reliable polarization reversal was achieved even with 1 μs pulses, with a tunneling electroresistance (TER) ratio of up to 10.4 (Figure 3f and Figure S19). Furthermore, endurance tests over 10^5 cycles maintained well-separated HRS and LRS states with no observable wake-up effect (Figure 3e), demonstrating robust fatigue resistance in the MoS_2/ReS_2 bilayer.

Sliding-Ferroelectric-Driven Field-Effect Biosensor

Building on the fast, reversible, and robust polarization switching demonstrated above, we implemented the MoS_2/ReS_2 heterojunction as the active channel in a ferroelectric field-effect transistor-based biosensor (bio-FeFET), creating a high-sensitivity, reconfigurable bioelectronic interface (Figure 4a). In this biosensor, polarization-induced fields can electrostatically enrich charged biomolecules and tune the interfacial charge distribution in situ. As a proof-of-concept, we fabricated a bio-FeFET for the label-free detection of 8-OHdG, an oxidative DNA damage biomarker, by functionalizing the channel with its specific aptamer. The sensing operation follows a "write−read−erase" logic, mirroring classical ferro-

https://doi.org/10.1021/acsnano.6c01271
ACS Nano XXXX, XXX, XXX−XXX

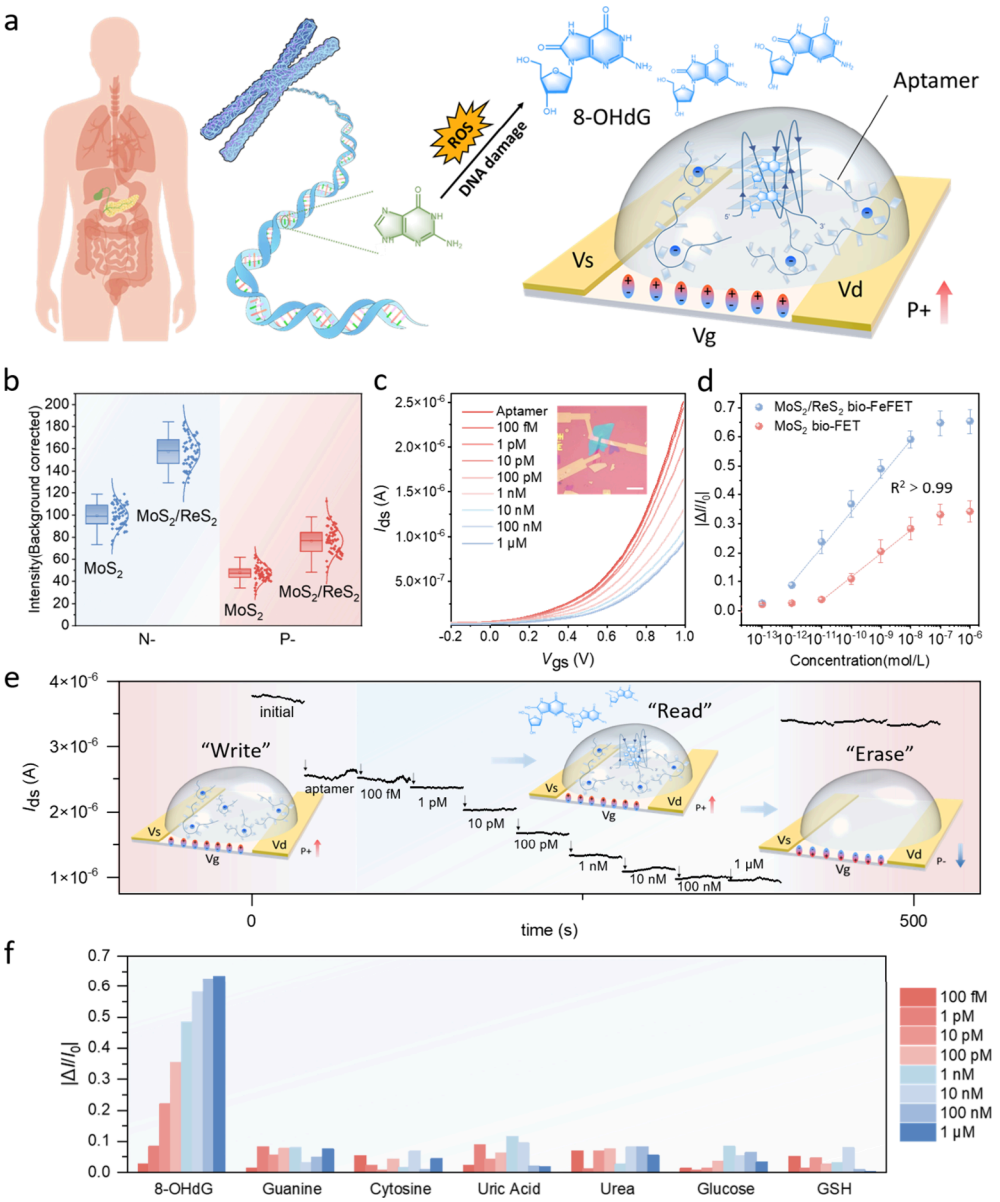

Figure 4. Prototype bio-FeFET platform for detecting 8-OHdG. (a) Schematic illustration of the biological origin of 8-OHdG and its detection using a bio-FeFET. (b) TOF-SIMS-based statistical comparison of nitrogen (N) and phosphorus (P) ion intensities in MoS_2/ReS_2 bio-FeFET and MoS_2 bio-FET devices, extracted from the first 100 s of ion sputtering. (c) Transfer characteristics of a representative MoS_2/ReS_2 bio-FeFET under exposure to increasing concentrations of 8-OHdG (100 fM to 1 μM). Inset: a corresponding optical image of the MoS_2/ReS_2 bio-FeFET, scale bar: 40 μm. (d) Sensitivity plot of normalized source-drain current change ($|\Delta I/I_0|$) versus logarithmic 8-OHdG concentration for both MoS_2/ReS_2 bio-FeFET and MoS_2-only bio-FET. (e) Reconfigurable "write−read−erase" operation of the MoS_2/ReS_2 bio-FeFET, with schematic insets highlighting each stage. During the write stage, upward polarization electrostatically attracts negatively charged aptamers to the channel surface, establishing a new baseline current. During the read stage, stepwise decreases in I_{ds} correspond to successive additions of 8-OHdG bound to the aptamers; each addition is followed by a 30 s $I-t$ measurement to monitor the real-time current response. During erase stage, reversing polarization and rinsing remove the aptamer−analyte complexes, restoring the current close to its initial level. (f) Specificity response of the MoS_2/ReS_2 bio-FeFET toward nontarget molecules including guanine, cytosine, uric acid, urea, glucose, and glutathione; each potential interferent is tested over the 100 fM to 1 μM concentration range.

electric memory and enabling programmable biosensing (Figure 4e).

During the "write" phase, a positive gate voltage exceeding the coercive field induces upward polarization of the MoS_2/ReS_2 heterojunction. This generates an out-of-plane electric field that attracts negatively charged aptamers to the channel surface. This polarization-driven aptamer enrichment was directly visualized by time-of-flight secondary ion mass spectrometry (TOF-SIMS). Compared to a MoS_2-only control, the MoS_2/ReS_2 device exhibited significantly stronger and more uniform nitrogen (N) and phosphorus (P) signals, key elemental markers of the aptamer backbone (Figures S20 and S21). Quantitative analysis further confirmed it, showing higher mean N (159 vs 99) and P (78 vs 57) counts in the heterobilayer (Figure 4b). The enhanced surface coverage of aptamers was further corroborated by complementary spectroscopic techniques. PL and Raman spectra exhibited a more pronounced PL blueshift and a redshift of the Raman A_{1g}

https://doi.org/10.1021/acsnano.6c01271
ACS Nano XXXX, XXX, XXX−XXX

mode in the polarized bio-FeFET, consistent with the expected effects of higher aptamer density and the associated p-type doping (Figures S22 and S23). This charge modulation was manifested directly in the electrical characteristics of the device. Coverage with the enriched aptamers resulted in a decreased drain current and a positive shift in the threshold voltage (Figure S24), which are electrical signatures of p-type doping induced by the negatively charged biomolecules.

Following aptamer immobilization, the device was operated in the "read" phase with a gate voltage below the coercive threshold. Upon exposure to 8-OHdG, the aptamer underwent a conformational change into a compact G-quadruplex structure, drawing its negative charge centers closer to the MoS_2 surface.[35,36] This enhanced the local electrostatic coupling and introduced additional p-doping, resulting in a further reduction in the drain current. As shown in Figure 4c, the drain-source current (I_{ds}) decreased systematically from 2.52 to 0.95 μA as the 8-OHdG concentration increased from 100 fM to 1 μM. The sensor response, defined as $|\Delta I_{ds}/I_0|$ (where I_0 is the baseline current after aptamer adsorption), was plotted against the logarithmic concentration of 8-OHdG (Figure 4d).[37−39] A linear calibration was obtained as $|\Delta I_{ds}/I_0| = 0.1257 \log_{10}C+1.6122$ with a high correlation coefficient. The corresponding sensitivity (12.57% per decade) was ~1.5-fold higher than that of a MoS_2 only control device (8.31% per decade). Based on a 3σ criterion with $\sigma = 0.025$, the LoD was estimated to be 5.6×10^{-13} M, underscoring the critical role of the MoS_2/ReS_2 ferroelectric heterobilayer. Furthermore, current−time ($I-t$) measurements demonstrated reproducible and stable responses (Figure 4e), confirming the operational robustness of the bio-FeFET.

The "erase" operation was realized by applying a negative gate voltage that reverses the ferroelectric polarization direction. This induced an upward internal electric field, electrostatically repelling the negatively charged aptamers and promoting their desorption from the MoS_2 surface. Subsequent rinsing restored the device to its baseline electrical state, enabling new detection cycles. As shown in Figure S25, the device exhibited good reusability over 10 consecutive write−read−erase cycles, consistently recovering over 80% of its initial current. Consistently, the PL response after the erase step also approached the initial state (Figure S26). This electrical regeneration eliminates the need for harsh chemical surface treatments and enables cost-effective and repeatable biosensing. Such reusability is particularly advantageous for point-of-care diagnostics and longitudinal health monitoring, where rapid turnaround and minimal device consumption are required.[40,41]

To evaluate the specificity of the MoS_2/ReS_2 bio-FeFET, we performed control experiments using a panel of potential interferents, including structurally similar nucleobases (guanine and cytosine) and common electroactive interferents in physiological fluids (uric acid, urea, glucose, and glutathione). Compared to the pronounced response toward the target 8-OHdG, these nontarget analytes induced negligible signal variation (Figure 4f and Figures S27−S32). The high specificity stems from the high binding affinity and structural selectivity of the aptamer toward 8-OHdG, further confirming the reliability of the bio-FeFET.

CONCLUSIONS

In summary, this work reports the discovery of sliding ferroelectricity in a lattice-mismatched MoS_2/ReS_2 heterobilayer. Through comprehensive structural, spectroscopic, and electrical characterizations, we confirmed the emergence of robust out-of-plane polarization featuring an ultrafast switching speed of 1 μs and an exceptional endurance of 10^5 cycles, establishing the system as an ideal candidate for constructing reconfigurable electronic interfaces. Leveraging these properties, we developed a bio-FeFET based on the MoS_2/ReS_2 heterobilayer for label-free and sensitive detection of 8-OHdG, an oxidative DNA damage biomarker. The device operates by harnessing the polarization field to electrostatically enrich negatively charged aptamer−analyte complexes at the interface. Our prototype device demonstrated a high sensitivity, a broad linear detection range spanning 5 orders of magnitude, and high specificity. Crucially, the fully electrical "write−read−erase" capability enables in situ biomolecule enrichment and interface regeneration, ensuring good reusability without the need for chemical regeneration. This work not only expands the material library for 2D sliding ferroelectrics but also establishes a versatile and scalable platform that seamlessly integrates high-speed logic operations with reconfigurable biochemical sensing for next-generation adaptive bioelectronics.

METHODS

Theoretical Calculations

First-principles calculations based on density functional theory (DFT) were performed using the Vienna Ab initio Simulation Package (VASP). The exchange-correlation interactions were treated within the generalized gradient approximation (GGA) using the Perdew−Burke−Ernzerhof (PBE) functional, and the long-range van der Waals interactions were included through dispersion corrections. The interactions between valence electrons and ionic cores were described using the projector-augmented wave (PAW) method with a kinetic energy cutoff of 600 eV. All atomic positions were relaxed using the conjugate-gradient scheme until the residual force on each atom was below 0.01 eV $Å^{-1}$, and the total energy convergence threshold was set to 10^{-7} eV. Brillouin zone sampling was carried out with a $7 \times 5 \times 1$ Monkhorst−Pack k-point grid. A vacuum spacing of >15 Å was applied along the out-of-plane direction to eliminate interlayer interactions. To avoid spurious electrostatic coupling between periodic images, a planar dipole correction was added at the center of the vacuum layer, as implemented in VASP.

Material Preparation

Monolayer MoS_2 and ReS_2 were synthesized separately via CVD. MoS_2 monolayers were grown on SiO_2/Si substrates following our previously reported procedure.[42] For ReS_2 growth, ReO_3 (~3 mg) was mixed thoroughly with molecular sieves to ensure a slow and uniform vapor release. Two fluorophlogopite mica substrates were arranged face-to-face, forming a confined space for growth. The system was heated under a flowing Ar atmosphere (100 sccm) to 200 °C over 10 min and held for 60 min. The temperature was then ramped to 850 °C over 23 min with Ar flow reduced to 70 sccm, maintaining this temperature for 10 min to enable the growth of monolayer ReS_2 (Figure S6). The parallel-stacked MoS_2/ReS_2 heterojunctions were assembled by using a polydimethylsiloxane-assisted dry transfer method under optical alignment. Monolayer MoS_2 was aligned on top of ReS_2 to ensure a near-zero twist angle. All transfer processes were performed in ambient conditions, and the stacked heterojunctions were annealed in Ar at 300 °C for 1 h to improve interfacial coupling without damaging the vdW interface integrity.

Microscopic and Spectroscopic Characterizations

Optical images were captured using a BX 51M microscope (Olympus). Raman and PL spectroscopic measurements were conducted with a HORIBA−Jobin−Yvon system utilizing a 532 nm

https://doi.org/10.1021/acsnano.6c01271
ACS Nano XXXX, XXX, XXX−XXX

laser at 1 mW power. AFM measurements were performed with a Dimension Icon instrument (Bruker) in tapping mode. TOF-SIMS measurements were carried out on an IONTOF M6. The HAADF-STEM images were obtained by using an aberration-corrected transmission electron microscope (Spectra 300, ThermoFisher Scientific Inc.) operated at 300 kV.

SHG Measurements

Optical SHG signals were collected using an inverted confocal microscope (Nikon, A1) with a femtosecond laser source (Coherent Co., Chameleon; a pulse width of 140 fs, a repetition rate of 80 MHz, and an output wavelength range of 700−1060 nm). The laser was modulated by laser power attenuation. After the attenuation plate was adjusted to regulate the laser power and the Galvano scanner, the beam entered the microscope and was focused onto a spot with an objective lens (40×, NA 0.95). The signal generated by the sample was collected through the same microscope objective, transmitted through a low-pass filter, and then entered the spectral detector unit with 32 channels. The wavelength detection range was 400−650 nm, with a wavelength resolution of 2.5 nm. Angle-dependent SHG signals were collected by using a Stanford SR830 DSP Lock-In Amplifier, which was coupled to a Light Conversion PHAROS femtosecond laser. The excitation source was ultrafast pulsed light at ∼1030 nm. A 20× objective lens was used to focus the laser, producing a spot diameter of about 5.5 μm. The sample was fixed, while the polarization of the incident light was rotated in 6° increments to obtain spectra at various angles.

PFM Measurements

Ferroelectric polarization of the MoS_2/ReS_2 heterojunction was examined using piezoresponse force microscopy (Bruker Dimension Icon) at room temperature. Measurements were carried out in resonance-enhanced mode using conductive Pt/Ir tips with a spring constant of 3 N/m. The resonance frequency for OOP measurement was set at ∼300 kHz. PFM hysteresis loops were recorded by applying a tip bias of ±8 V to the samples.

C-AFM Measurements

C-AFM measurements of the MoS_2/ReS_2 heterojunction were conducted by using a Cypher atomic force microscope at room temperature. Measurements were carried out in ORCA-AFM mode with a grounded holder using the HQ: NSC18/Pt tips with a spring constant of 2.8 N m^{-1}. The Ti/Pt film with a thickness of 10 nm/40 nm was deposited on SiO_2/Si using an electron-beam evaporator. MoS_2/ReS_2 samples were transferred to the conductive substrate by poly(methyl methacrylate) (PMMA)-assisted transfer method (Figure S13).

Fabrication and Measurements of FTJ Devices

Monolayer graphene was mechanically exfoliated onto a SiO_2/Si substrate. Following this, a MoS_2/ReS_2 heterojunction was placed on top of the graphene with the aid of PMMA and PDMS using a fixed-point transfer setup. PDMS and PMMA were subsequently removed from the bilayer by being heated at 85 °C and soaked in acetone, respectively. Finally, a 10 nm Cr/30 nm Au electrode was fabricated on the MoS_2/ReS_2 heterojunction using EBL, thermal evaporation, and lift-off, resulting in a ferroelectric tunnel junction device, with the MoS_2/ReS_2 heterojunction serving as the vertical channel, and graphene and metal electrode serving as the bottom and top electrodes, respectively. The electrical transport properties were measured in a probe station equipped with a Keysight B1500A semiconductor analyzer under vacuum (10^{-5} mbar) at room temperature. The fatigue analysis was measured in a probe station equipped with a Keysight B1530 semiconductor analyzer at room temperature.

Construction and Modification of Bio-FeFET Devices

Graphene was exfoliated onto SiO_2/Si substrates with prefabricated markers, followed by the deterministic transfer of hexagonal boron nitride (hBN) onto the graphene bottom electrode. Subsequently, ReS_2 and MoS_2 flakes were sequentially transferred to hBN using the same transfer setup. Finally, a 10 nm In/30 nm Au electrode was fabricated on the MoS_2/ReS_2 bilayer using EBL, thermal evaporation, and lift-off, resulting in a bottom-gated ferroelectric-based bio-FET with MoS_2/ReS_2 serving as the channel, and graphene and In/Au electrode as the bottom gate and source/drain electrodes, respectively. The 8-OHdG aptamer−ssDNA[43] was diluted to 10 μM with 10 mM Tris-HCl buffer (pH 7.4). To fold the aptamer into its functional secondary structure, the solution was heated at 95 °C for 5 min and cooled slowly to room temperature. Next, 2 μL of the aptamer solution was dropped onto the polarized channel surface, followed by rinsing with PBS and drying with nitrogen gas to remove nonelectrostatically bound aptamers. After drying with nitrogen, the formed sensing surface was further incubated with 1 μL of 8-OHdG solution (MedChemExpress, 10 fM to 10 μM), and the transfer characteristics were recorded.

■ ASSOCIATED CONTENT

Supporting Information

The Supporting Information is available free of charge The Supporting Information is available free of charge at https://pubs.acs.org/doi/10.1021/acsnano.6c01271.

Sliding process of MoS_2/ReS_2 heterojunction, spontaneous OOP polarization value and relative energy, interlayer differential charge density, dipole value of AA-up and AA-down configurations, lattice mismatch calculation, synthesis and characterization of monolayer ReS_2, AES analysis of MoS_2/ReS_2 heterojunction, typical PL spectra of the MoS_2/ReS_2 heterojunction bilayer, atomic-scale structure of MoS_2/ReS_2 heterojunction, angle-resolved SHG intensities of monolayer ReS_2 and MoS_2/ReS_2 heterojunction, relationship between SHG intensity and pump power, schematic diagram for the fabrication process of C-AFM testing samples, C-AFM characterization of polarization switching, schematic diagram of the preparation process of PFM samples, evolution of morphology, amplitude and phase images, out-of-plane PFM testing of monolayer MoS_2 and ReS_2, dynamic switching characteristics of the FTJ, time-of-flight secondary ion mass spectrometry, photoluminescence signature, Raman spectroscopic probing, transfer curves, reusability test, and specificity tests (PDF)

■ AUTHOR INFORMATION

Corresponding Authors

Changming Ke − *Department of Physics, School of Science, Westlake University, Hangzhou 310030, China;* orcid.org/0000-0002-2018-2441; Email: kechangming@westlake.edu.cn

Yaming Zhou − *Key Laboratory of Organic Optoelectronics and Molecular Engineering of the Ministry of Education, Department of Chemistry, Tsinghua University, Beijing 100084, China*; Email: ymzhou@mail.tsinghua.edu.cn

Liying Jiao − *Key Laboratory of Organic Optoelectronics and Molecular Engineering of the Ministry of Education, Department of Chemistry, Tsinghua University, Beijing 100084, China;* orcid.org/0000-0002-6576-906X; Email: lyjiao@mail.tsinghua.edu.cn

Authors

Weijia Mu − *Key Laboratory of Organic Optoelectronics and Molecular Engineering of the Ministry of Education, Department of Chemistry, Tsinghua University, Beijing 100084, China*

https://doi.org/10.1021/acsnano.6c01271
ACS Nano XXXX, XXX, XXX−XXX

Ning Guo − *CAS Key Laboratory of Standardization and Measurement for Nanotechnology, National Center for Nanoscience and Technology, Beijing 100190, China*
Zheng Zhang − *College of Materials Science and Engineering, Fuzhou University, Fuzhou 350108, China*
Lei Yang − *College of Biological and Chemical Engineering, Qilu Institute of Technology, Jinan 250000, China;* orcid.org/0000-0003-2153-3570
Zhewei Li − *Key Laboratory of Organic Optoelectronics and Molecular Engineering of the Ministry of Education, Department of Chemistry, Tsinghua University, Beijing 100084, China*
Jing Li − *Key Laboratory of Photochemical Conversion and Optoelectronic Materials, Technical Institute of Physics and Chemistry, Chinese Academy of Sciences, Beijing 100190, China;* orcid.org/0000-0002-0227-0392
Shufang Yue − *Key Laboratory of Organic Optoelectronics and Molecular Engineering of the Ministry of Education, Department of Chemistry, Tsinghua University, Beijing 100084, China*
Jingying Zheng − *College of Materials Science and Engineering, Fuzhou University, Fuzhou 350108, China;* orcid.org/0000-0002-7790-4775
Qiang Zheng − *CAS Key Laboratory of Standardization and Measurement for Nanotechnology, National Center for Nanoscience and Technology, Beijing 100190, China;* orcid.org/0000-0002-9279-7779
Shi Liu − *Department of Physics, School of Science, Westlake University, Hangzhou 310030, China;* orcid.org/0000-0002-8488-4848

Complete contact information is available at: https://pubs.acs.org/10.1021/acsnano.6c01271

Author Contributions

The manuscript was written through contributions of all authors. All authors have given approval to the final version of the manuscript.

Notes

The authors declare no competing financial interest.

■ ACKNOWLEDGMENTS

L.J. acknowledges support from the National Key R&D Program of China (nos. 2021YFA1200102 and 2022YFA1103403) and the National Natural Science Foundation of China (grant no. 22275111). C.K. acknowledges support from the National Natural Science Foundation of China (grant no. 12304128) and the computational resources provided by the Westlake HPC Center. The authors thank the Nanofab Lab of National Center for Nanoscience and Technology for the assistance in device fabrication.

■ REFERENCES

(1) Li, L.; Wu, M. Binary compound bilayer and multilayer with vertical polarizations: Two-dimensional ferroelectrics, multiferroics, and nanogenerators. *ACS Nano* **2017**, *11* (6), 6382−6388.
(2) Wu, M.; Li, J. Sliding ferroelectricity in 2D van der Waals materials: Related physics and future opportunities. *Proc. Natl. Acad. Sci. U. S. A.* **2021**, *118* (50), No. e2115703118.
(3) Ji, J.; Yu, G.; Xu, C.; Xiang, H. J. General theory for bilayer stacking ferroelectricity. *Phys. Rev. Lett.* **2023**, *130* (14), No. 146801.
(4) Vizner Stern, M.; Salleh Atri, S.; Ben Shalom, M. Sliding van der Waals polytypes. *Nat. Rev. Phys.* **2025**, *7* (1), 50−61.
(5) Gong, Y.; Duan, R.; Hu, Y.; Wu, Y.; Zhu, S.; Wang, X.; Wang, Q.; Lau, S. P.; Liu, Z.; Tay, B. K. Reconfigurable and nonvolatile ferroelectric bulk photovoltaics based on 3R-WS_2 for machine vision. *Nat. Commun.* **2025**, *16* (1), 230.
(6) Wang, C.; You, L.; Cobden, D.; Wang, J. Towards two-dimensional van der Waals ferroelectrics. *Nat. Mater.* **2023**, *22* (5), 542−552.
(7) Wang, X.; Yasuda, K.; Zhang, Y.; Liu, S.; Watanabe, K.; Taniguchi, T.; Hone, J.; Fu, L.; Jarillo-Herrero, P. Interfacial ferroelectricity in rhombohedral-stacked bilayer transition metal dichalcogenides. *Nat. Nanotechnol.* **2022**, *17* (4), 367−371.
(8) Meng, P.; Wu, Y.; Bian, R.; Pan, E.; Dong, B.; Zhao, X.; Chen, J.; Wu, L.; Sun, Y.; Fu, Q.; Liu, Q.; Shi, D.; Zhang, Q.; Zhang, Y. W.; Liu, Z.; Liu, F. Sliding induced multiple polarization states in two-dimensional ferroelectrics. *Nat. Commun.* **2022**, *13* (1), 7696.
(9) Wang, Y.; Zeng, Z.; Tian, Z.; Li, C.; Braun, K.; Huang, L.; Li, Y.; Luo, X.; Yi, J.; Wu, G.; Liu, G.; Li, D.; Zhou, Y.; Chen, M.; Wang, X.; Pan, A. Sliding ferroelectricity induced ultrafast switchable photovoltaic response in ϵ-InSe layers. *Adv. Mater.* **2024**, *36* (44), No. 2410696.
(10) Sui, F.; Jin, M.; Zhang, Y.; Qi, R.; Wu, Y.-N.; Huang, R.; Yue, F.; Chu, J. Sliding ferroelectricity in van der Waals layered γ-InSe semiconductor. *Nat. Commun.* **2023**, *14* (1), 36.
(11) Sui, F.; Li, H.; Qi, R.; Jin, M.; Lv, Z.; Wu, M.; Liu, X.; Zheng, Y.; Liu, B.; Ge, R.; Wu, Y. N.; Huang, R.; Yue, F.; Chu, J.; Duan, C. Atomic-level polarization reversal in sliding ferroelectric semiconductors. *Nat. Commun.* **2024**, *15* (1), 3799.
(12) Rogée, L.; Wang, L.; Zhang, Y.; Cai, S.; Wang, P.; Chhowalla, M.; Ji, W.; Lau, S. P. Ferroelectricity in untwisted heterobilayers of transition metal dichalcogenides. *Science* **2022**, *376* (6596), 973−978.
(13) Wan, Y.; Hu, T.; Mao, X.; Fu, J.; Yuan, K.; Song, Y.; Gan, X.; Xu, X.; Xue, M.; Cheng, X.; Huang, C.; Yang, J.; Dai, L.; Zeng, H.; Kan, E. Room-temperature ferroelectricity in 1T'-ReS_2 multilayers. *Phys. Rev. Lett.* **2022**, *128* (6), No. 067601.
(14) Mu, W.; Ke, C.; Huangfu, C.; Dong, J.; Zhou, Y.; Zheng, J.; Yue, S.; Li, J.; Liu, S.; Jiao, L. Room-temperature out-of-plane ferroelectricity in 1T'/1H MoS_2 heterophase bilayer. *Adv. Mater.* **2025**, *37* (29), No. e2504941.
(15) Bian, R.; He, R.; Pan, E.; Li, Z.; Cao, G.; Meng, P.; Chen, J.; Liu, Q.; Zhong, Z.; Li, W.; Liu, F. Developing fatigue-resistant ferroelectrics using interlayer sliding switching. *Science* **2024**, *385* (6704), 57−62.
(16) Li, X.; Qin, B.; Wang, Y.; Xi, Y.; Huang, Z.; Zhao, M.; Peng, Y.; Chen, Z.; Pan, Z.; Zhu, J.; Cui, C.; Yang, R.; Yang, W.; Meng, S.; Shi, D.; Bai, X.; Liu, C.; Li, N.; Tang, J.; Liu, K.; et al. Sliding ferroelectric memories and synapses based on rhombohedral-stacked bilayer MoS_2. *Nat. Commun.* **2024**, *15* (1), 10921.
(17) Jin, Q.; Men, K.; Li, G.; Ou, T.; Lian, Z.; Deng, X.; Zhao, H.; Zhang, Q.; Ming, A.; Wei, Q.; Wei, F.; Tu, H. Ultrasensitive graphene field-effect biosensors based on ferroelectric polarization of lithium niobate for breast cancer marker detection. *ACS Appl. Mater. Interfaces* **2024**, *16* (22), 28896−28904.
(18) Hahm, J. Y.; Park, J.; Jang, E. S.; Chi, S. W. 8-Oxoguanine: from oxidative damage to epigenetic and epitranscriptional modification. *Exp. Mol. Med.* **2022**, *54* (10), 1626−1642.
(19) Cooke, M. S.; Evans, M. D.; Dizdaroglu, M.; Lunec, J. Oxidative DNA damage: mechanisms, mutation, and disease. *FASEB J.* **2003**, *17* (10), 1195−1214.
(20) Vizner Stern, M.; Waschitz, Y.; Cao, W.; Nevo, I.; Watanabe, K.; Taniguchi, T.; Sela, E.; Urbakh, M.; Hod, O.; Ben Shalom, M. Interfacial ferroelectricity by van der Waals sliding. *Science* **2021**, *372* (6549), 1462−1466.
(21) Lee, C.; Yan, H.; Brus, L. E.; Heinz, T. F.; Hone, J.; Ryu, S. Anomalous lattice vibrations of single- and few-layer MoS_2. *ACS Nano* **2010**, *4* (5), 2695−2700.
(22) Zhang, J.; Wang, J.; Chen, P.; Sun, Y.; Wu, S.; Jia, Z.; Lu, X.; Yu, H.; Chen, W.; Zhu, J.; Xie, G.; Yang, R.; Shi, D.; Xu, X.; Xiang, J.; Liu, K.; Zhang, G. Observation of strong interlayer coupling in MoS_2/WS_2 heterostructures. *Adv. Mater.* **2016**, *28* (10), 1950−1956.

(23) Cui, F.; Wang, C.; Li, X.; Wang, G.; Liu, K.; Yang, Z.; Feng, Q.; Liang, X.; Zhang, Z.; Liu, S.; Lei, Z.; Liu, Z.; Xu, H.; Zhang, J. Tellurium-assisted epitaxial growth of large-area, highly crystalline ReS_2 atomic layers on mica substrate. *Adv. Mater.* **2016**, *28* (25), 5019−5024.
(24) Jiang, J.; Wang, X.; Wang, D.; Chai, Y.; Yang, Y.; Ding, L.; Guo, X.; Li, A.; Xu, T.; Huang, H.; Zhou, S.; Luo, Z.; Zhang, J.; Ouyang, F.; Ding, F.; Wang, Z.-J.; Wang, S. Chirality-transferred epitaxy of circular polarization-sensitive ReS_2 monolayer single crystals. *Nat. Commun.* **2025**, *16* (1), 7119.
(25) Mak, K. F.; Lee, C.; Hone, J.; Shan, J.; Heinz, T. F. Atomically thin MoS_2: a new direct-gap semiconductor. *Phys. Rev. Lett.* **2010**, *105* (13), No. 136805.
(26) Wang, Z.; Luo, R.; Johnson, I.; Kashani, H.; Chen, M. Inlaid ReS_2 quantum dots in monolayer MoS_2. *ACS Nano* **2020**, *14* (1), 899−906.
(27) Hong, X.; Kim, J.; Shi, S. F.; Zhang, Y.; Jin, C.; Sun, Y.; Tongay, S.; Wu, J.; Zhang, Y.; Wang, F. Ultrafast charge transfer in atomically thin MoS_2/WS_2 heterostructures. *Nat. Nanotechnol.* **2014**, *9* (9), 682−686.
(28) Kumar, N.; Najmaei, S.; Cui, Q.; Ceballos, F.; Ajayan, P. M.; Lou, J.; Zhao, H. Second harmonic microscopy of monolayer MoS_2. *Phys. Rev. B* **2013**, *87* (16), No. 161403.
(29) Song, Y.; Hu, S.; Lin, M.-L.; Gan, X.; Tan, P.-H.; Zhao, J. Extraordinary Second Harmonic Generation in ReS_2 Atomic Crystals. *ACS Photonics* **2018**, *5* (9), 3485−3491.
(30) Xu, M.; Ji, H.; Zhang, M.; Zheng, L.; Li, W.; Luo, L.; Chen, M.; Liu, Z.; Gan, X.; Wang, X.; Huang, W. CVD synthesis of twisted bilayer WS_2 with tunable second harmonic generation. *Adv. Mater.* **2024**, *36* (19), No. 2313638.
(31) Li, Z.; Huang, J.; Zhou, L.; Xu, Z.; Qin, F.; Chen, P.; Sun, X.; Liu, G.; Sui, C.; Qiu, C.; Lu, Y.; Gou, H.; Xi, X.; Ideue, T.; Tang, P.; Iwasa, Y.; Yuan, H. An anisotropic van der Waals dielectric for symmetry engineering in functionalized heterointerfaces. *Nat. Commun.* **2023**, *14* (1), 5568.
(32) Hsu, W.-T.; Zhao, Z.-A.; Li, L.-J.; Chen, C.-H.; Chiu, M.-H.; Chang, P.-S.; Chou, Y.-C.; Chang, W.-H. Second harmonic generation from artificially stacked transition metal dichalcogenide twisted bilayers. *ACS Nano* **2014**, *8* (3), 2951−2958.
(33) Vasudevan, R. K.; Balke, N.; Maksymovych, P.; Jesse, S.; Kalinin, S. V. Ferroelectric or non-ferroelectric: Why so many materials exhibit "ferroelectricity" on the nanoscale. *Appl. Phys. Rev.* **2017**, *4* (2), No. 021302.
(34) Zhao, P.; Wang, R.; Lien, D. H.; Zhao, Y.; Kim, H.; Cho, J.; Ahn, G. H.; Javey, A. Scanning probe lithography patterning of monolayer semiconductors and application in quantifying edge recombination. *Adv. Mater.* **2019**, *31* (48), No. 1900136.
(35) Weaver, S.; Mohammadi, M. H.; Nakatsuka, N. Aptamer-functionalized capacitive biosensors. *Biosens. Bioelectron.* **2023**, *224*, No. 115014.
(36) Liu, H.; Wang, Y.-S.; Tang, X.; Yang, H.-X.; Chen, S.-H.; Zhao, H.; Liu, S.-D.; Zhu, Y.-F.; Wang, X.-F.; Huang, Y.-Q. A novel fluorescence aptasensor for 8-hydroxy-2'-deoxyguanosine based on the conformational switching of K^+-stabilized G-quadruplex. *J. Pharm. Biomed. Anal.* **2016**, *118*, 177−182.
(37) Sakata, T. Signal transduction interfaces for field-effect transistor-based biosensors. *Commun. Chem.* **2024**, *7* (1), 35.
(38) Fakih, I.; Durnan, O.; Mahvash, F.; Napal, I.; Centeno, A.; Zurutuza, A.; Yargeau, V.; Szkopek, T. Selective ion sensing with high resolution large area graphene field effect transistor arrays. *Nat. Commun.* **2020**, *11* (1), 3226.
(39) Dai, C.; Liu, Y.; Wei, D. Two-dimensional field-effect transistor sensors: The road toward commercialization. *Chem. Rev.* **2022**, *122* (11), 10319−10392.
(40) Jiang, Z.; Ye, D.; Xiang, L.; He, Z.; Dai, X.; Yang, J.; Xiong, Q.; Ma, Y.; Zhi, D.; Zou, Y.; Peng, Q.; Wang, S.; Li, J.; Zhang, F.; Di, C. A. A drug-mediated organic electrochemical transistor for robustly reusable biosensors. *Nat. Mater.* **2024**, *23* (11), 1547−1555.
(41) Zargartalebi, H.; Mirzaie, S.; GhavamiNejad, A.; Ahmed, S. U.; Esmaeili, F.; Geraili, A.; Flynn, C. D.; Chang, D.; Das, J.; Abdrabou, A.; Sargent, E. H.; Kelley, S. O. Active-reset protein sensors enable continuous in vivo monitoring of inflammation. *Science* **2024**, *386* (6726), 1146−1153.
(42) Zheng, J.; Yan, X.; Lu, Z.; Qiu, H.; Xu, G.; Zhou, X.; Wang, P.; Pan, X.; Liu, K.; Jiao, L. High-mobility multilayered MoS_2 flakes with low contact resistance grown by chemical vapor deposition. *Adv. Mater.* **2017**, *29* (13), No. 1604540.
(43) Miyachi, Y.; Shimizu, N.; Ogino, C.; Fukuda, H.; Kondo, A. Selection of a DNA aptamer that binds 8-OHdG using GMP-agarose. *Bioorg. Med. Chem. Lett.* **2009**, *19* (13), 3619−3622.

https://doi.org/10.1021/acsnano.6c01271
ACS Nano XXXX, XXX, XXX−XXX